BOLETIN DE LA SOCIEDAD ESPAÑOLA DE
Cerámica y Vidrio
www.elsevier.es/bsecv

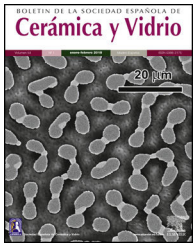

Original

A first insight into the microstructure and crack propagation in novel boron nitride nanosheet/3YTZP composites

Carmen Muñoz-Ferreiro[a], *Ana Morales-Rodríguez*[a], *Ángela Gallardo-López*[a], *Rosalía Poyato*[b,*]

[a] *Dpto. de Física de la Materia Condensada, ICMS, CSIC-Universidad de Sevilla, Apdo. 1065, 41080 Sevilla, Spain*
[b] *Inst. Ciencia de Materiales de Sevilla, ICMS, CSIC-Universidad de Sevilla, Américo Vespucio 49, 41092 Sevilla, Spain*

ARTICLE INFO

Article history:
Received 8 October 2019
Accepted 21 February 2020
Available online 17 March 2020

Keywords:
BN nanosheets
3YTZP
Composite materials
Mechanical properties

ABSTRACT

In this work, novel 3 mol% yttria tetragonal zirconia polycristalline (3YTZP) ceramic composites with boron nitride nanosheets (BNNS) are investigated for the first time. Highly densified composites with 1 and 4 vol% BNNS were obtained by spark plasma sintering (SPS) after BNNS synthesis using a solution exfoliation method and BNNS dispersion into the ceramic powder by ultrasonication. The BNNS presented homogeneous distribution throughout the ceramic matrix and preferential alignment in the plane perpendicular to the pressing axis during SPS. The BNNS incorporation had practically no effect on the Vickers hardness of the material nor on the Young's modulus. Anisotropy in crack development was found in the composite with 4% vol BNNS, together with a mechanism of extensive microcracking. Several energy-absorbing mechanisms during crack propagation, such as crack deflection, crack bridging, crack branching, BNNS pull-out and BNNS debonding, were identified in the composites by a close observation of the indentation-induced fracture paths.

Una primera visión de la microestructura y la propagación de fisuras en novedosos compuestos de 3YTZP con nanoláminas de nitruro de boro

Palabras clave:
Nanoláminas de nitruro de boro
Circona
Materiales compuestos
Propiedades mecánicas

RESUMEN

En este trabajo, se han investigado por primera vez unos novedosos compuestos cerámicos de circona tetragonal policristalina con 3 mol% de itria con nanoláminas de nitruro de boro. Tras la síntesis de las nanoláminas usando un método de exfoliación en solución y su dispersión en el polvo cerámico mediante la aplicación de ultrasonidos, se han obtenido compuestos altamente densos con 1 y 4% vol de nanoláminas mediante *spark plasma sintering*. Las nanoláminas presentaron una distribución homogénea en la matriz cerámica y una

* *Corresponding author.*
E-mail address: rosalia.poyato@icmse.csic.es (R. Poyato).
https://doi.org/10.1016/j.bsecv.2020.02.003

alineación preferencial en el plano perpendicular al eje de presión durante el *spark plasma sintering*. Su incorporación en la matriz cerámica no tuvo prácticamente ningún efecto sobre la dureza Vickers del material ni sobre su módulo de Young. En el compuesto con 4 vol% de nanoláminas se observaron tanto anisotropía en el desarrollo de las fisuras como un mecanismo de microfisuración extensiva. Mediante una observación minuciosa de las grietas inducidas por indentación se han identificado diferentes mecanismos de absorción de energía durante la propagación de las fisuras, tales como desviación, puenteo o ramificación de fisuras y arranque o decohesión de nanoláminas.

Introduction

In the last decade, the extraordinary properties of graphene have motivated intense research on this nanomaterial pursuing its use in a wide range of applications [1]. In particular, the use of graphene nanosheets as fillers in ceramics allows the obtaining of composites with enhanced toughness and tailored thermal and electrical properties with potential interest for structural and functional applications [2]. More recently, other two-dimensional (2D) nanomaterials – known as inorganic graphene analogs, IGAs – as MoS_2, WS_2 and BN [3] have appeared on the scientific scene because they show common properties with graphene and analog structure, while presenting some advantages. One of the IGAs that has awakened a higher interest is two-dimensional boron nitride (2D-BN) [4,5], also known as "white graphene" because of its white color. This nanomaterial presents high surface area and mechanical properties similar to the observed ones in graphene, with a high Young's modulus of 700–900 GPa [6]. One of the most interesting features of this nanomaterial is its enhanced oxidation resistance in comparison with graphene, as it can sustain temperatures up to 850 °C [7]. Thus, ceramic composites incorporating 2D-BN as a second phase are promising materials for high temperature applications, where graphene ceramic composites are degraded. Moreover, its white color confers the potential to be used as reinforcement material in dental applications without modifying the implant color. Although studies about the biocompatibility of ceramic composites with BNNS have not been published until now, a study from Lahiri et al. [8] on hydroxyapatite reinforced with boron nitride nanotubes (BNNT) has shown a suitable biocompatibility together with enhancements on toughness and wear-resistance properties. This would open the door to an extended range of applications of ceramic composites with BN nanostructures in biomedicine.

Although ceramic composites with boron nitride nanosheets (BNNS) as fillers appear as highly attractive materials, the studies on these composites are up to date very scarce. Yue et al. [9] studied ZrB_2–SiC composites with a combination of BNNS and BNNT prepared by SPS, and described the synergetic toughening mechanisms of both 1D and 2D BN nanomaterials promoting enhancements on the mechanical properties. Saggar et al. [10] studied the incorporation of BNNS on an amorphous borosilicate glass matrix. The BNNS were prepared using a liquid-exfoliation method and SPS was used for densification. They reported enhancements on the fracture toughness and the flexure strength with increasing BNNS content. Lee et al. [11] studied Si_3N_4 composites with BN nanoplatelets (BNNP) and reported enhancements on fracture toughness, strength and wear resistance when incorporating 2 vol% BNNP. The nanoplatelets were synthesized by means of high-energy planetary ball milling, dispersed with the ceramic powders using a surfactant and then consolidated by hot pressing. Also, very recently Sun et al. [12,13] studied hot pressed fused silica composites with BNNP. In a first study [13], they found enhancements on flexural strength and fracture toughness when incorporating just 0.5 wt% BNNP. The BNNP were synthesized by solution exfoliation and dispersed in fused silica powder using a surfactant-free flocculation method. However, nanoplatelet agglomeration was observed for BNNP contents higher than 0.5 wt%. In a more recent work [12], these authors used a surface modification assisted flocculation method with the aim of solving the problem of agglomeration for contents higher than 0.5 wt%, and extended the enhancements on mechanical properties to a content of 1.5 wt% BNNP. The toughening mechanisms were identified by microstructural observations as crack bridging and deflection along with BNNP pull-out. Alumina composites with 1.0 wt% BNNS fabricated by a flocculation method and hot pressing were recently studied by Wang et al. [14]. The BNNS were prepared by a liquid-exfoliation method and the employment of the flocculation process prompted the homogeneous dispersion of the BNNS in the alumina matrix, resulting in an enhancement of the bending strength.

To the best of our knowledge, no studies have been published on zirconia composites with BNNS. Zirconia-based ceramics are well known for their high-temperature and structural applications, as well as for their use in dentistry and orthopedics [15,16]. It is expected that the performance in these different applications would be enhanced by the incorporation of BNNS, in view of the improvements of flexural strength and fracture toughness reported for BNNT reinforced zirconia composites [17,18].

In this study, 3YTZP composites reinforced with 1 and 4 vol% BNNS are investigated for the first time. The BNNS were synthesized by a solution exfoliation method and dispersed into the ceramic powder by ultrasonication. The effects of the BNNS incorporation on the densification, microstructure and mechanical properties of the spark plasma sintered composites were investigated. Several energy-absorbing crack propagation hindering mechanisms present in the composites

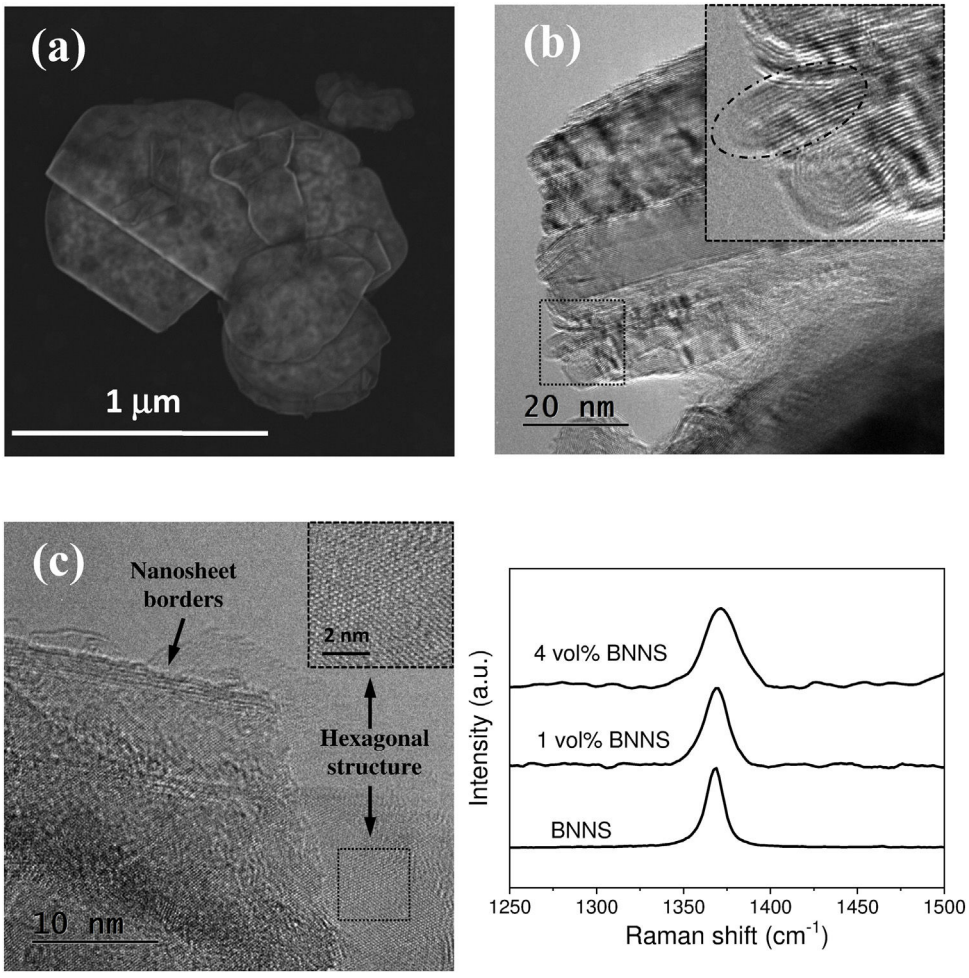

Fig. 1 – (a) HRSEM, and (b and c) HRTEM images of the synthesized BNNS, (d) Raman spectra of the synthesized BNNS and the BNNS/3YTZP composites.

were identified by a close observation of the indentation-induced fracture paths.

Experimental procedure

Materials processing

Synthesis and characterization of the BN nanosheets

The BNNS were obtained by the liquid-exfoliation method [13,19], using hexagonal BN powder (*h*-BN, 99.5% purity, particle size ≤44 μm, Alfa Aesar, Kandel, Germany) and a solution of ethanol/water with 55% ethanol volume fraction as dispersion solvent. 300 mg of the powder were suspended in 100 ml of solvent and bath sonicated (Sonorex Digitec DT 255, Bandelin, Germany) for 10 h. The obtained suspensions were centrifuged (Rotofix 32A, Hettich, Germany) at 3000 rpm for 20 min to remove powder aggregates. The dispersions were immediately frozen with liquid nitrogen and then freeze-dried for 48 h in order to avoid re-agglomeration of the obtained nanosheets during drying (Cryodos-80, Telstar, Terrasa, Spain, Centro de Investigación, Tecnología e Innovación de la Universidad de Sevilla, CITIUS).

The morphology of the BNNS was characterized by high-resolution scanning electron microscopy (HRSEM, S5200, Hitachi High-Technologies America Inc., USA, CITIUS). Transmission electron microscopy (TEM) characterization was also performed in the BNNS. To that end, a few droplets of the sonicated BNNS suspension were deposited on a Cu transmission grid with C coating and, after drying, the BNNS were observed in a FEI-Tecnai field-emission gun scanning transmission electron microscope (STEM-FEG), mod. G2 F30 with an S-Twin objective lent, operated at 300 kV, with 0.2 nm point resolution (Instituto de Ciencia de Materiales de Sevilla, ICMS).

Processing and sintering of the ceramic composites

The synthesized BNNS were re-dispersed in the 55% ethanol/water solution by bath sonication (Sonorex Digitec DT 255, Bandelin, Germany) for 30 min. Composite powders with 1 and 4 vol% BNNS content were prepared by adding the corresponding quantity of 3YTZP ceramic powder to the BNNS suspension. The mixtures were further sonicated for 5 min and dried on a hot plate with continuous magnetic stirring. The resulting powders were homogenized in an agatha mortar.

Table 1 – Density, Young's modulus and Vickers hardness of the BNNS/3YTZP composites.

Sample	ρ_{exp} (g/cm^3)	ρ_{rel} (%)	E (GPa)	H_V (GPa)	
				In-plane	Cross-section
3YTZP	6.1[a]	100[a]	208 ± 12	13.9 ± 0.5	–
1 vol% BNNS	5.96 ± 0.04	99.1 ± 0.6	186 ± 12	14.5 ± 2.0	14.1 ± 1.6
4 vol% BNNS	5.87 ± 0.03	99.4 ± 0.8	197 ± 13	13.0 ± 2.0	13.2 ± 1.4

[a] Data from a monolithic 3YTZP ceramic prepared from the same powder and with the same sintering conditions [21] have been added in order to establish a comparison.

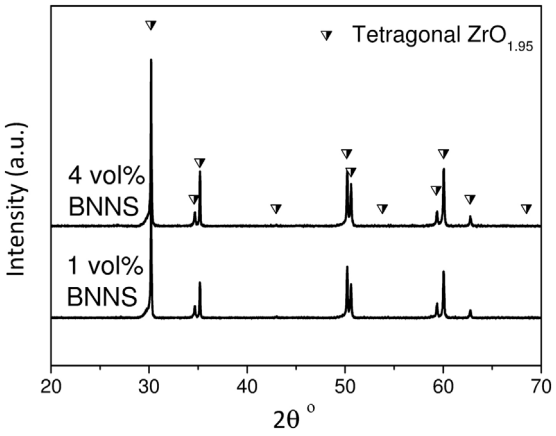

Fig. 2 – X-ray diffraction patterns of the BNNS/3YTZP composites.

The composite powders were loaded into a 15 mm diameter graphite mold. A sheet of graphite paper was placed between the powders and the die/punches to ensure their electrical, mechanical and thermal contact. Graphitic paper was also placed along the inner wall of the die for easy removal of the sample. Spark Plasma Sintering (Model 515S, SPS Dr Sinter Inc., Kanagawa, Japan, CITIUS) was performed in vacuum at 1250 °C for 5 min under a uniaxial pressure of 75 MPa, with 200 °C/min heating and 50 °C/min cooling ramps. The temperature was measured by means of an optical pyrometer focused on the side of the graphite die. The sintered composites of cylindrical shape with a ~15 mm diameter and a height of ~2 mm were manually ground to eliminate the surface graphite from the SPS molding system.

Microstructural characterization

The bulk density of the composites was measured with the Archimedes' method using distilled water. The theoretical density was calculated using the rule of mixtures, considering $\rho = 6.05\ g\,cm^{-3}$ for the 3YTZP and $\rho = 2.1\ g\,cm^{-3}$ for the BNNS.

Raman spectroscopy was used to confirm the existence of the BNNS in the sintered materials. The spectra were obtained using a dispersive microscope (Horiba Jobin Yvon LabRam HR800, Kyoto, Japan, ICMS) equipped with a He-Ne green laser (532.14 nm) at 20 mW. The microscope used a 100× objective

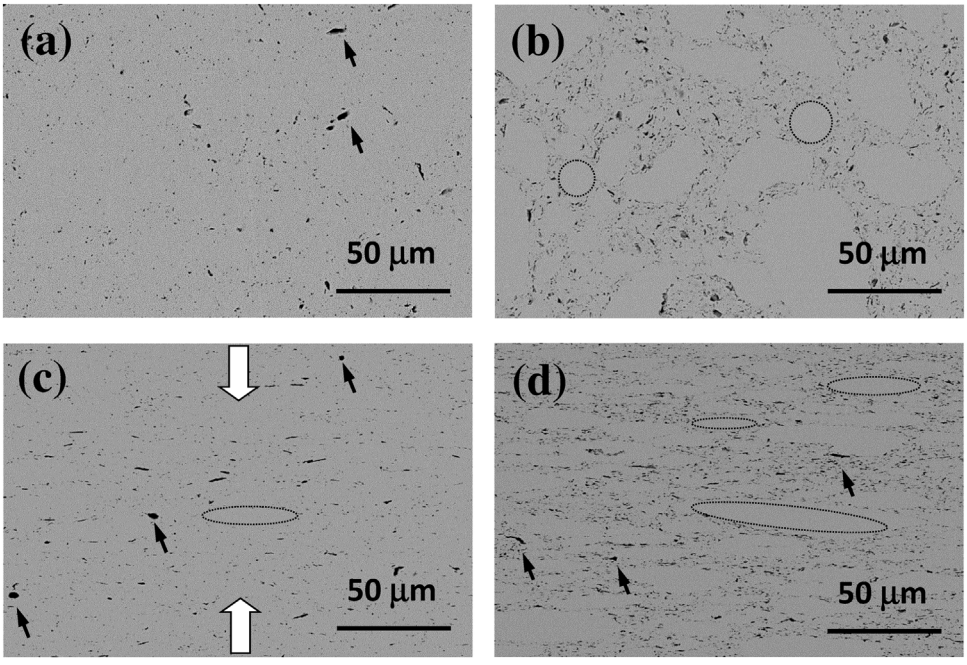

Fig. 3 – Backscattered scanning electron (BSE) microscopy images from the composites i.p. (a, b) and c.s. (c, d) polished surfaces: (a and c) 1 vol%, (b and d) 4 vol% BNNS. Compression axis during SPS is indicated in (c) by arrows.

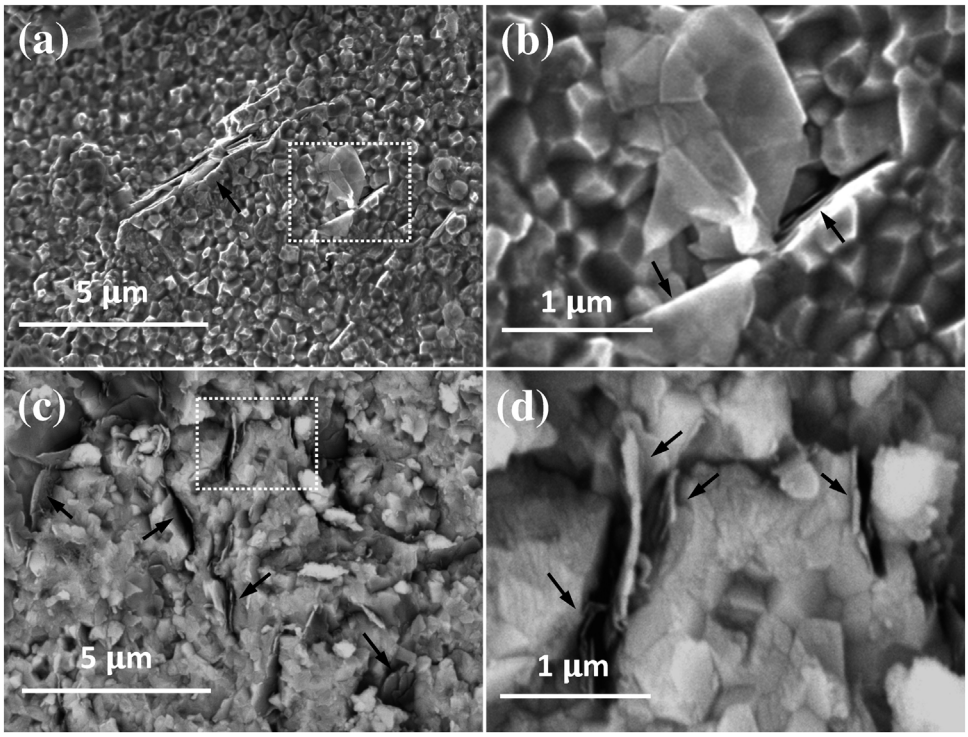

Fig. 4 – High–resolution SEM images of the fracture surfaces of the composites with (a and b) 1 vol%, (c and d) 4 vol% BNNS. The images in (b) and (d) show high magnification of the selected areas in (a) and (c), respectively.

and a confocal pinhole of 100 µm. The Raman spectrometer was calibrated using a silicon wafer.

Identification of the crystallographic phases on the sintered composites was carried out by X-ray diffraction (XRD, model D8 Advance A25, Bruker Co. Massachusetts, USA, CITIUS). To characterize the distribution of the BNNS in the zirconia matrix, and to account for any structural anisotropy of the composites, cross-section (c.s.) and in-plane (i.p.) surfaces, i.e. surfaces parallel and perpendicular to the SPS pressing axis, were polished with diamond paste up to 1 µm and analyzed by low magnification conventional SEM (FEI-Teneo, FEI, USA, CITIUS) using backscattered electrons (BSE) for imaging. The fracture surfaces of the composites were also examined by HRSEM (S5200 Hitachi, CITIUS) to observe the distribution and morphology of the BNNS incorporated to the ceramic matrix.

Mechanical characterization

The Young's modulus of the composites was measured using the impulse excitation technique (Sonelastic, ATCP Physical Engineering, Brasil) to assess the influence of the BNNS content on the elastic properties of the composites.

The hardness of the composites was evaluated on the polished i.p. and c.s. surfaces to account for any possible anisotropy, with a Vickers micro-indenter (Duramin Struers, Germany) and loads of 1.96 N applied for 10 s. At least 10 indentations were analyzed for each composite, sufficiently separated from each other to avoid overlapping the stress fields and to avoid border effects.

Higher loads (9.087 N) were also applied for 10 s with a Wilson indenter (VH 1150, Buehler, Illinois, USA) on the polished i.p. and c.s. surfaces of the composites to create fractures from the corner of the imprints. These cracks were subsequently observed by SEM (FEI-Teneo, CITIUS) with the aim of identifying how the BNNS modify the crack propagation mechanisms. This microscope has an associated software (MAPS) that allows to scan large surfaces with high resolution and afterwards performs the assembly of the final images.

Results

Microstructural characterization of the synthesized BNNS

The as-synthesized BNNS present a two dimensional structure with submicrometric lateral size (Fig. 1a). The BNNS lateral dimensions, taking as length value the major axis of the nanosheet, were in the range of 400–700 nm for most of the BNNS, although nanosheets from ~100 nm up to 2–3 µm were also observed. BNNS thickness of ~10–60 nm could be estimated from TEM images where the nanosheets appear sidewise. However, HRTEM analysis revealed that these thicknesses could be actually related to the stacking of several BNNS (Fig. 1b shows a BN platelet that is likely formed by several BNNS with 15–20 nm thickness each). Furthermore, the folded edges of some nanosheets were observed (marked in Fig. 1c), so the nanosheets could be even thinner. The stacking could have been created during the deposition of the suspension on the grid. The measured interplanar space of the BNNS was 0.329 nm, which is close to the reported values for BN nanoplatelets (0.34 nm) [11] and for *h*-BN crystals (0.333 nm) [4]. The SAED (selected area electron diffraction)

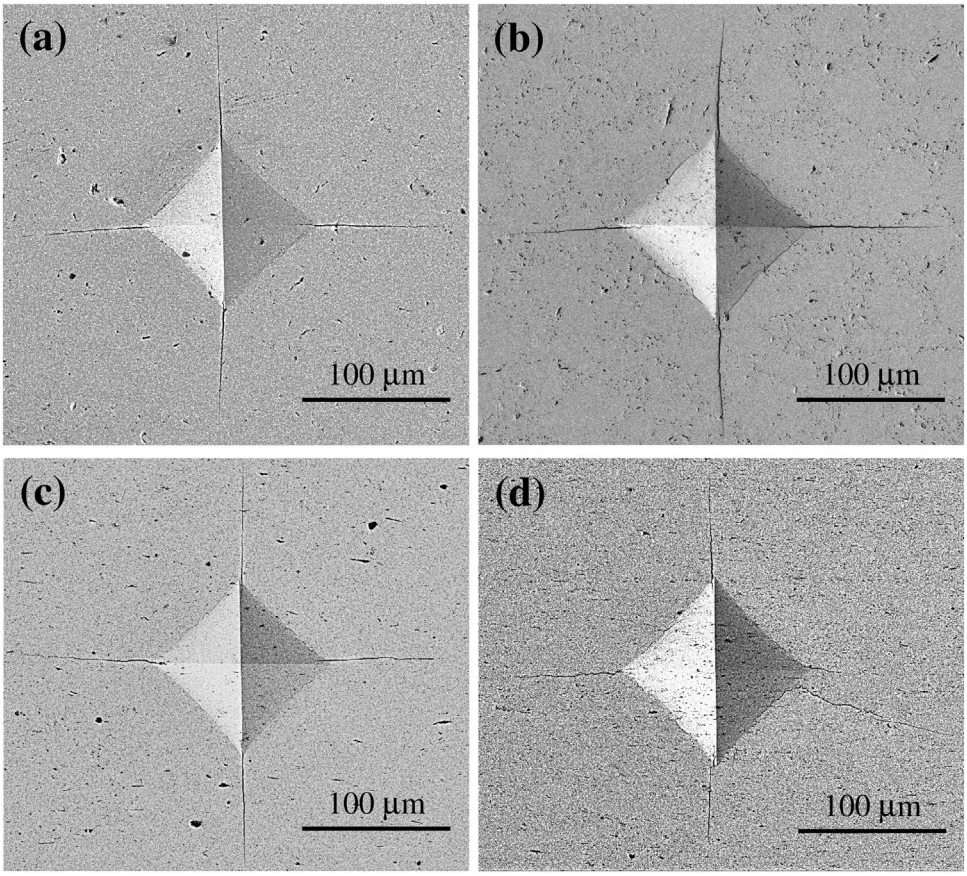

Fig. 5 – SEM images of the composites i.p. (a, b) and c.s. (c, d) surfaces after Vickers indentation at 9.087 N: (a and c) 1 vol%, (b and d) 4 vol% BNNS.

pattern revealed a hexagonal symmetry (Fig. 1c), so the BNNS maintained the hexagonal structure after the synthesis process. Fig. 1c also shows some individual few layered BNNS with thickness lower than 5 nm.

Microstructural characterization of the composites

The Raman spectra acquired on the sintered composites (Fig. 1d) showed a unique Raman peak at 1365 cm^{-1}, which is associated with the E_{2G} vibration mode [5]. The detection of this characteristic Raman peak [7,11,20] confirms the existence of the nanosheets without significant structural damage in the composites after sintering.

A high densification was achieved for both composites, with 99.1 ± 0.6 and 99.4 ± 0.8% relative densities for 1 and 4 vol% BNNS, respectively (Table 1). The obtaining of composites near 100% theoretical density highlights the adequacy of the sintering conditions selected in this study. The XRD patterns of the sintered composites (Fig. 2) reveal that the main crystallographic phase in both materials is the reduced tetragonal zirconia ($ZrO_{1.95}$, JCPDS 01-081-1544). This reduction is consequence of the highly reducing atmosphere during the sintering process, carried out in vacuum and with a graphite mold containing the powders. The peak with the highest intensity ($\theta \sim 30.2^{\circ}$) shows a widening on the left side, indicating that there is a small contribution of the solid solution of zirconia and yttria, $Zr_{0.80}Y_{0.20}O_{1.9}$, with cubic structure (JCPDS 01-082-1246) [21].

The homogeneity in the distribution of the BN nanosheets throughout the ceramic matrix is illustrated by low-magnification BSE-SEM on the polished i.p. and c.s. surfaces of the composites (Fig. 3). The light phase observed in the micrographs corresponds to the zirconia matrix while the dark phase corresponds to the BNNS. This clear distinction is consequence of the average atomic number difference between them. The c.s. surfaces of both composites (Fig. 3c and d) reveal a preferential alignment of the *ab* plane of the BNNS in the plane perpendicular to the pressing axis during SPS. Thus, these images show a side view of the nanosheets, which have maintained the two-dimensional character after processing and sintering, with a clear alignment. However, on the i.p. surface of the composites a random orientation of the BNNS is observed (Fig. 3a and b). Thus, both composites present structural anisotropy, consequence of the intrinsic 2D character of the nanosheets, together with their preferential alignment due to the uniaxial pressure applied during sintering. In both composites, most BNNS appear rather uniformly distributed throughout the ceramic matrix with scarce agglomerates (marked with arrows in Fig. 3). Some BNNS-free ceramic areas can also be observed, being this fact more remarkable for the composite with 4 vol% BNNS. These areas are the result of the inadequate mixing of the ceramic powder

and the BN nanosheets during the composite powder processing. Therefore, processing efforts shall be carried out to avoid their formation in future works.

The fracture surfaces of the sintered composites (Fig. 4) reveal an intergranular fracture mode with the BNNS dispersed in the matrix and mainly isolated, although some stackings formed by several nanosheets can also be observed. Most of the BNNS present a lateral size lower than 1 μm, in accordance with the HRSEM observations of the as-synthesized BN nanosheets (Fig. 1a). The BNNS appear as flat, rigid structures situated, in most cases, at the ceramic grain boundaries. Nevertheless, some of them present wrinkles or are lying on top of the fracture surface of the composite. Several BNNS pull-outs can also be observed, associated with pits or cavities between the BNNS and the ceramic grains, on both sides of the nanosheet or at least on one of the sides. This could be due to the generation of porosity during the cooling step in the composite sintering process, as a consequence of the thermal expansion coefficient mismatch of the two phases [22]. However, the high densification achieved for the composites (Table 1) discards this option.

Mechanical characterization of the composites

The Young's modulus of the composites, reported in Table 1, slightly decreases with respect to the monolithic 3YTZP. The slight decrease of density in the composites with respect to the ceramic could be responsible for this effect. However, no significant differences are observed between the values corresponding to the two composites with 1 and 4 vol% BNNS contents. A similar trend of the Young's modulus with the BNNS content has been reported for composites with an amorphous borosilicate glass matrix [10]. In this previous study, similar Young's modulus for the composites and the pure glass were reported, probably consequence of their similar density values.

The Vickers hardness values, measured on the i.p. and c.s. surfaces of both composites, are also presented in Table 1. It can be observed that the incorporation of the BNNS has practically no effect on the Vickers hardness of the material, with no significant change in comparison with the corresponding value for the monolithic 3YTZP ceramic. The same effect has been previously reported for boron nitride nanoplatelet (BNNP) reinforced Si_3N_4 nanocomposites [11] and for plasma sprayed hydroxyapatite coatings incorporating BNNP [20]. Moreover, no significant differences are found between the hardness values acquired on the i.p. and the c.s. surfaces for none of the two composites.

Fig. 5 shows the Vickers indentations performed on the i.p. and c.s. surfaces of the composites at high loads with the aim to generate fractures from the corners of the imprints. All the imprints present the typical cracks of brittle materials, arising from the four vertices of the indentation – two horizontal and two vertical ones – independently of being performed on the i.p. or the c.s. surface. The composite with 1 vol% BNNS presents an isotropic crack development, with similar mean crack lengths measured for both surfaces (~84 ± 10 μm). However, for the composite with 4 vol% BNNS, anisotropy in the crack formation and propagation is found. Whereas crack lengths similar to the ones on the composite with 1 vol%

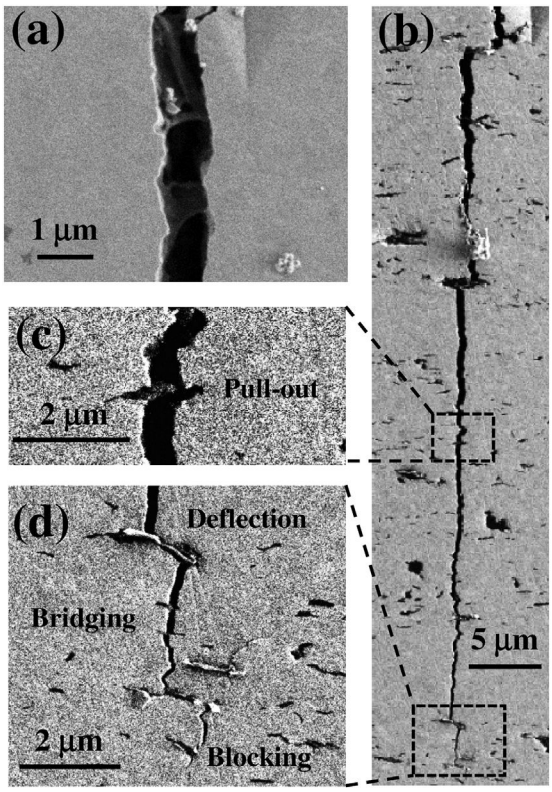

Fig. 6 – SEM images showing vertical indentation-induced cracks on the i.p. (a) and c.s. (b) surfaces of the composite with 4 vol% BNNS. The images in (c) and (d) show high magnification of the selected areas in (b), revealing energy dissipation mechanisms: (c) BNNS pull-out, (d) crack deflection, bridging and blocking by BNNS.

BNNS are measured on the i.p. surface, it is observed that the imprints performed on the c.s. surface present multiple small cracks close to the horizontal axis (i.e. perpendicular to the SPS pressing axis). These cracks do not arise from the corners of the imprints, but from the indentation edges, and propagate along the BNNS/matrix interface (Fig. 5d). Usually, extensive microcracking around indentations is considered as an energy dissipating mechanism. In this case, the dissipation of energy is evidenced by a significant shortening of the length of the cracks that arise from the vertices in the vertical direction (67 ± 13 μm). The occurrence of extensive microcracking made impossible to measure the length of the cracks in the horizontal direction. Moreover, in some imprints, no cracks arising from the corners in this direction were found.

Analyzing the fracture paths of the Vickers indentation cracks can help identifying possible crack propagation hindering mechanisms related to the incorporation of the BNNS into the zirconia matrix. To that end, the indentation-induced fracture paths have been observed in SEM for the composite with 4 vol% BNNS (Figs. 6 and 7). The images reveal evidence of several energy-absorbing mechanisms that could hinder the crack propagation. In the c.s. surface, when the crack is perpendicular to the direction of the preferential alignment of the BNNS, several nanosheets that bridge and deflect the crack in a perpendicular way can be observed (Fig. 6b–d). Crack bridging

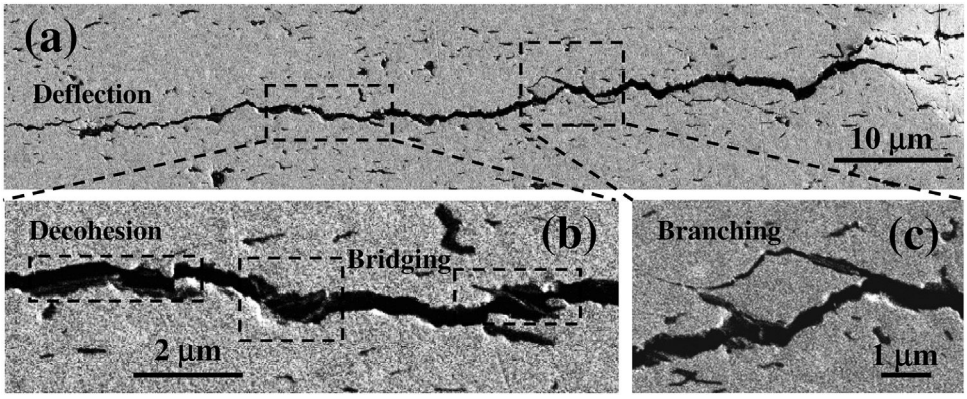

Fig. 7 – (a) SEM image showing a horizontal indentation-induced crack on the c.s. surface of the composite with 4 vol% BNNS. (b and c) High magnification SEM images of the selected areas in (a), revealing BNNS debonding, crack branching, deflection and bridging.

by BNNS can be also observed in the composite i.p. surface (Fig. 6a). In this case, the *ab* plane of the BNNS is observed bridging the crack. In fact, the crack deflection by BNNS results in a tortuous fracture path (Fig. 6d) which usually requires more energy to propagate. The crack deflection mechanisms and, thus, the tortuosity of the fracture paths increase with the BNNS content (Fig. 5) and is more evident in the direction where the BNNS are aligned – perpendicular to the pressing axis during sintering (Fig. 5d). It has been reported that crack deflection by sheet-like reinforcement is more effective than by tubular-like reinforcement [9,23].

Another mechanisms that can dissipate the crack propagation energy such as crack branching (Fig. 7c), BNNS pull-out (Fig. 6c) and BNNS debonding (Fig. 7b) can also be observed. A close observation of the fracture path (Fig. 7b) reveals the clear decohesion of the BNNS, with some BN layers remaining attached to one side of the crack whereas the rest of the BNNS stays attached to the other side. This BNNS debonding can also be observed in the high magnification images of the fracture surface (Fig. 4b and d), where it is shown that the outmost layers of the BNNS remain attached to the ceramic matrix whereas the inner nanosheets have been pulled-out. As it has been suggested by Sun et al. [12,13] and Saggar et al. [10] there is a strong interaction between the BNNS and the ceramic matrix while the van der Waals interactions between the nanosheets are very weak, which results in an easier inter-layer sliding and pull-out of the inner nanosheets. This inter-layer sliding could result in a toughening mechanism based on inter-layer friction [24] as described by Sun et al. [13]. Although this toughening mechanism has also been observed in systems reinforced with graphene [25], it has been suggested [13] that in the case of composites with BNNS, the inter-layer movements of the BN sheets may consume more energy in comparison with graphene, as a consequence of the intrinsic structure of 2D-BN. The friction between the BN layers that form the BNNS during sliding and debonding could result in an enhanced mechanism of energy dissipation during the fracture of the material. A certain level of interfacial bonding that allows frictional sliding is a key condition for enhanced toughening [26]. Furthermore, the fracture energy dissipated by BNNS pull-out or debonding phenomena could be highly dependent on the type of interfacial bonding, as previously stated for graphene-ceramic composites [26,27].

Toughness measurements of the composites under study are still necessary to validate with macroscopic data the effectiveness of the microstructural energy dissipation mechanisms during crack propagation shown in this work on the enhancement of the mechanical properties. Furthermore, deep and systematic TEM studies of the BNNS/3YTZP interfacial characteristics are needed to evaluate the bonding strength, key in load transport between matrix and filler, and will be carried out in further investigations.

Conclusions

In summary, highly densified novel 3YTZP composites with 1 and 4 vol% BNNS were successfully obtained by SPS. The composites presented structural anisotropy, with a preferential alignment of the *ab* plane of the BNNS perpendicular to the pressing axis during SPS, and a homogeneous distribution of the BN nanosheets throughout the ceramic matrix. The incorporation of the BNNS had no remarkable effect on the Vickers hardness nor on the Young's modulus of the material. However, a mechanism of extensive microcracking, together with anisotropy in the crack formation and propagation, was observed in the composite with 4 vol% BNNS. Several efficient energy-absorbing crack propagation hindering mechanisms, such as crack deflection, crack bridging, crack branching, BNNS pull-out and BNNS debonding, were identified in the fracture paths of the BNNS/3YTZP composites.

Acknowledgments

Financial support from project PGC-2018-101377-B-100 (MCIU/AEI/FEDER, UE) is acknowledged. The authors greatly acknowledge Dr. T.C. Rojas (ICMS) for performing the TEM images.

REFERENCES

[1] K.S. Novoselov, V.I. Fal'ko, L. Colombo, P.R. Gellert, M.G. Schwab, K. Kim, A roadmap for graphene, Nature 490 (2012) 192–200, http://dx.doi.org/10.1038/nature11458.

[2] P. Miranzo, M. Belmonte, M.I. Osendi, From bulk to cellular structures: a review on ceramic/graphene filler composites, J. Eur. Ceram. Soc. 37 (2017) 3649–3672.

[3] A.C. Ferrari, et al., Science and technology roadmap for graphene, related two-dimensional crystals, and hybrid systems, Nanoscale 7 (2015) 4598–4810, http://dx.doi.org/10.1039/c4nr01600a.

[4] K. Zhang, Y. Feng, F. Wang, Z. Yang, J. Wang, Two dimensional hexagonal boron nitride (2D-hBN): synthesis, properties and applications, J. Mater. Chem. C 5 (2017) 11992–12022, http://dx.doi.org/10.1039/c7tc04300g.

[5] R.V. Gorbachev, I. Riaz, R.R. Nair, R. Jalil, L. Britnell, B.D. Belle, E.W. Hill, K.S. Novoselov, K. Watanabe, T. Taniguchi, A.K. Geim, P. Blake, Hunting for monolayer boron nitride: Optical and Raman signatures, Small 7 (2011) 465–468, http://dx.doi.org/10.1002/smll.201001628.

[6] D. Lee, S.H. Song, J. Hwang, S.H. Jin, K.H. Park, B.H. Kim, S.H. Hong, S. Jeon, Enhanced mechanical properties of epoxy nanocomposites by mixing noncovalently functionalized boron nitride nanoflakes, Small 9 (2013) 2602–2610, http://dx.doi.org/10.1002/smll.201203214.

[7] L.H. Li, J. Cervenka, K. Watanabe, T. Taniguchi, Y. Chen, Strong oxidation resistance of atomically thin boron nitride nanosheets, ACS Nano 8 (2014) 1457–1462, http://dx.doi.org/10.1021/nn500059s.

[8] D. Lahiri, V. Singh, A.P. Benaduce, S. Seal, L. Kos, A. Agarwal, Boron nitride nanotube reinforced hydroxyapatite composite: mechanical and tribological performance and in-vitro biocompatibility to osteoblasts, J. Mech. Behav. Biomed. Mater. 4 (2011) 44–56, http://dx.doi.org/10.1016/j.jmbbm.2010.09.005.

[9] C. Yue, W. Liu, L. Zhang, T. Zhang, Y. Chen, Fracture toughness and toughening mechanisms in a (ZrB_2–SiC) composite reinforced with boron nitride nanotubes and boron nitride nanoplatelets, Scr. Mater. 68 (2013) 579–582, http://dx.doi.org/10.1016/j.scriptamat.2012.12.005.

[10] R. Saggar, H. Porwal, P. Tatarko, I. Dlouhý, M.J. Reece, Boron nitride nanosheets reinforced glass matrix composites, Adv. Appl. Ceram. 114 (2015) S26–S33, http://dx.doi.org/10.1179/1743676115Y.0000000056.

[11] B. Lee, D. Lee, J.H. Lee, H.J. Ryu, S.H. Hong, Enhancement of toughness and wear resistance in boron nitride nanoplatelet (BNNP) reinforced Si_3N_4 nanocomposites, Sci. Rep. 6 (2016) 27609, http://dx.doi.org/10.1038/srep27609.

[12] G. Sun, J. Bi, W. Wang, J. Zhang, Enhancing mechanical properties of fused silica composites by introducing well-dispersed boron nitride nanosheets, Ceram. Int. 44 (2018) 5002–5009, http://dx.doi.org/10.1016/j.ceramint.2017.12.096.

[13] G. Sun, J. Bi, W. Wang, J. Zhang, Microstructure and mechanical properties of boron nitride nanosheets-reinforced fused silica composites, J. Eur. Ceram. Soc. 37 (2017) 3195–3202, http://dx.doi.org/10.1016/j.jeurceramsoc.2017.03.029.

[14] W. Wang, G. Sun, Y. Chen, X. Sun, J. Bi, Preparation and mechanical properties of boron nitride nanosheets/alumina composites, Ceram. Int. 44 (2018) 21993–21997, http://dx.doi.org/10.1016/j.ceramint.2018.08.314.

[15] R.C. Garvie, R.H. Hannink, R.T. Pascoe, Ceramic steel? Nature 258 (1975) 703–704, http://dx.doi.org/10.1038/258703a0.

[16] S. Saridag, O. Tak, G. Alniacik, Basic properties and types of zirconia: an overview, World J. Stomatol. 2 (2013) 40–47.

[17] J.-J. Xu, Y.-J. Bai, W.-L. Wang, S.-R. Wang, F.-D. Han, Y.-X. Qi, J.-Q. Bi, Toughening and reinforcing zirconia ceramics by introducing boron nitride nanotubes, Mater. Sci. Eng. A 546 (2012) 301–306, http://dx.doi.org/10.1016/j.msea.2012.03.077.

[18] P. Tatarko, S. Grasso, Z. Chlup, H. Porwal, M. Kašiarová, I. Dlouhý, M.J. Reece, Toughening effect of multi-walled boron nitride nanotubes and their influence on the sintering behaviour of 3Y-TZP zirconia ceramics, J. Eur. Ceram. Soc. 34 (2014) 1829–1843, http://dx.doi.org/10.1016/j.jeurceramsoc.2013.12.046.

[19] K. Zhou, N. Mao, H. Wang, Y. Peng, H. Zhang, A mixed-solvent strategy for efficient exfoliation of inorganic graphene analogues, Angew. Chem. Int. Ed. 50 (2011) 10839–10842.

[20] J. Zhu, Y. Chen, J. Ren, D. Zhao, W. Liu, Boron nitride nanoplatelets induced synergetic strengthening and toughening effects on splats and their boundaries of plasma sprayed hydroxyapatite coatings, Ceram. Int. 44 (2018) 10604–10610, http://dx.doi.org/10.1016/j.ceramint.2018.03.085.

[21] A. Gallardo-López, I. Márquez-Abril, A. Morales-Rodríguez, A. Muñoz, R. Poyato, Dense graphene nanoplatelet/yttria tetragonal zirconia composites: processing, hardness and electrical conductivity, Ceram. Int. 43 (2017) 11743–11752, http://dx.doi.org/10.1016/j.ceramint.2017.06.007.

[22] S. Turan, K.M. Knowles, High resolution transmission electron microscopy of the planar defect structure of hexagonal boron nitride, Phys. Status Solid. 150 (1995) 227–237.

[23] M.A. Rafiee, J. Rafiee, I. Srivastava, Z. Wang, H. Song, Z. Yu, N. Koratkar, Fracture and fatigue in graphene nanocomposites, Small 6 (2010) 179–183.

[24] J.Y. Park, S. Kwon, J.H. Kim, Nanomechanical and charge transport properties of two-dimensional atomic sheets, Adv. Mater. Interfaces 1 (2014) 1300089.

[25] I. Ahmad, M. Islam, H.S. Abdo, T. Subhani, K.A. Khalil, A.A. Almajid, B. Yazdani, Y. Zhu, Toughening mechanisms and mechanical properties of graphene nanosheet-reinforced alumina, Mater. Des. 88 (2015) 1234–1243, http://dx.doi.org/10.1016/j.matdes.2015.09.125.

[26] C. Ramirez, P. Miranzo, M. Belmonte, M.I. Osendi, P. Poza, S.M. Vega-Diaz, M. Terrones, Extraordinary toughening enhancement and flexural strength in Si_3N_4 composites using graphene sheets, J. Eur. Ceram. Soc. 34 (2014) 161–169, http://dx.doi.org/10.1016/j.jeurceramsoc.2013.08.039.

[27] C. Muñoz-Ferreiro, A. Morales-Rodríguez, T.C. Rojas, E. Jiménez-Piqué, C. López-Pernía, R. Poyato, A. Gallardo-López, Microstructure, interfaces and properties of 3YTZP ceramic composites with 10 and 20 vol% different graphene-based nanostructures as fillers, J. Alloys Compd. 777 (2019) 213–224, http://dx.doi.org/10.1016/j.jallcom.2018.10.336.